

# Design and Modeling of Magnetolectric Micro-Particles for Neuromodulation

Ram Prasad Narayanan

Walton Institute for Information and Communication Systems  
Science

South East Technological University  
Waterford, Ireland

[Ram.Narayanan@WaltonInstitute.ie](mailto:Ram.Narayanan@WaltonInstitute.ie)

ORCID: 0000-0002-4947-5993

Ali Khaleghi

Institute of Electronic Systems

Norwegian University of Science and Technology

Trondheim, Norway

[ali.khaleghi@ntnu.no](mailto:ali.khaleghi@ntnu.no)

ORCID: 0000-0002-8372-1529

**Abstract**— This paper presents a novel approach to neural stimulation using magnetolectric microparticles (MEMPs), potentially transforming biostimulation methods. We employ multi-physics modeling to integrate MEMPs into a simulation framework, focusing on designing spherical core-shell structures. These structures exploit resonant modes and the nonlinearity of magnetostrictive materials to amplify deformation under high-frequency magnetic fields. This process effectively down-converts remotely applied high-frequency signals into low-frequency deformations, crucial for neural stimulation. The interaction between the magnetostrictive core and the piezoelectric shell, particularly under resonance, enhances mechanical-to-electrical energy conversion, elevating bio-stimulation capabilities. Our findings suggest a path towards more efficient, targeted, and minimally invasive neural stimulation, with implications for advancing biomedical engineering and neuroscience.

**Keywords**— Magnetolectric Microparticles, Neural Stimulation, Magneto-Mechanical Resonance, Nonlinear Biostimulation, Wireless Biomedical Devices

## I. INTRODUCTION (HEADING 1)

The field of neural stimulation, or neurostimulation, stands at the forefront of medical innovation, fundamentally affecting the lives of millions globally. Neurostimulation encompasses various therapies that utilize electrical stimulation to modulate neural function [1], [2], [3]. These therapies range from invasive to non-invasive approaches and have shown efficacy in treating diverse conditions, including movement disorders, epilepsy, pain, and depression [4], [5], [6]. Recent advancements have seen significant progress in neural stimulation techniques. Transcranial Direct Current Stimulation (tDCS) and Transcranial Magnetic Stimulation (TMS) represent new therapeutic options for a range of disorders [7], [8]. In particular, deep Brain Stimulation (DBS) has become a pivotal method in managing diseases like Parkinson's and essential tremors. However, despite their efficacy, these methods confront issues related to precision and invasiveness, which can affect long-term effectiveness. Fig. 1 illustrates the different types of stimulation.

A fundamental challenge within the field is the use of implantable electrodes. While central to neurostimulation technologies, these devices are associated with tissue damage and often face limitations in achieving precise neural stimulation patterns. Emerging technologies like optogenetics, efficient in single neuron resolution, encounter challenges related to genetic modification and limited depth of light penetration in biological tissues [9]. Material-based approaches like Magnetic Nanoparticle (MNP) based thermal modulation and Magnetolectric Nanoparticles (MENP) are another approach. MENPs can convert magnetic fields into

electrical stimuli but face low-frequency source reliance, which demands bulky applicators and hinders single-particle control.

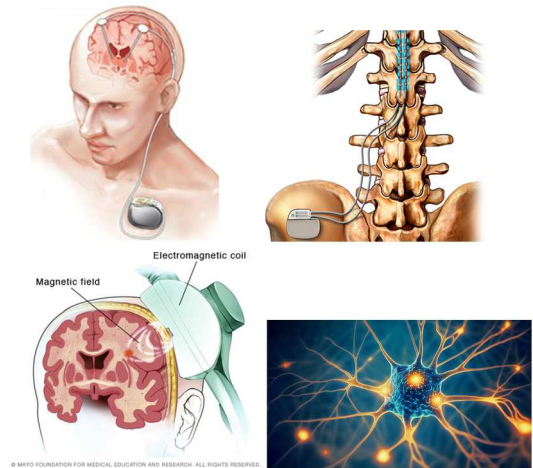


Fig. 1. Deep brain stimulation using battery-powered electrodes, Spinal cord wired electrical stimulation, Non-invasive TMS noninvasive magnetic induction stimulator, and Optogenetics light triggered stimulation.

Exploring magnetolectric (ME) materials has emerged as a groundbreaking approach in the quest for refined neurostimulation techniques. These materials, capable of transducing magnetic signals into electrical outputs, present a promising avenue for wireless, non-invasive neural stimulation [10], [11], [12], [13], [14]. This paper delves into the innovative use of ME microparticles (MEMPs), introducing a novel methodology with the potential to transform bio stimulation practices. Central to our study is the detailed multi-physics modelling of these ME particles within a numerical finite element method framework, aimed at comprehensively simulating their magneto-mechanical and mechano-electric properties. We specifically focus on the design and functionality of spherical core-shell ME particles, where the geometry plays a critical role in enhancing particle deformation under high-frequency magnetic fields, further amplified by the non-linear properties of magnetostrictive materials.

## II. MATERIALS AND METHODS

### A. Magnetolectric Physics

Magnetostriction, a phenomenon in ferromagnetic materials, manifests as strain induced by applied magnetic fields. This strain arises from the reorientation and perturbation of electron spins, causing lattice deformation in the ferromagnetic structures. It's the interaction of magnetic and elastic forces that makes magnetostriction a valuable property for energy conversion [15]. Fig. 2 shows the

The project is funded by NTNU Health Seed fund Grant No. 980001110, and project Brain-Connected inteRFace TO machineS (B-CRATOS) under grant #965044, Horizon 2020 FET-OPEN.

magnetolectric effect in a core shell particle. When coupled with a piezoelectric domain, this allows for the conversion of generated elastic forces into electrical fields.

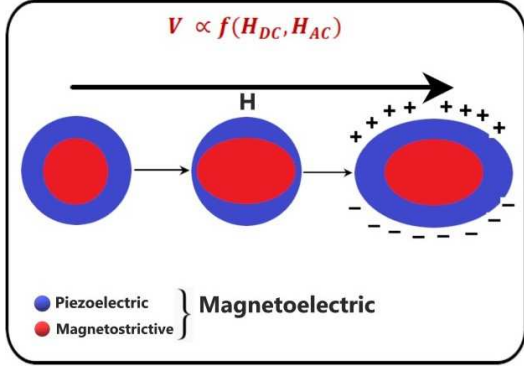


Fig. 2. Magnetolectric effect in a coreshell particle

This process is governed by the Joule and Villari effect, described by the equations [16]:

$$\sigma = C\epsilon - e^T E - q^T H, \quad (1)$$

$$D = e\epsilon + kE + \alpha H, \quad (2)$$

$$B = q\epsilon + \alpha E + \mu H, \quad (3)$$

where,  $C$  is the elastic stiffness tensor,  $e$  and  $q$  are the piezoelectric and piezomagnetic constant tensors respectively,  $k$  and  $\mu$  are the electric permittivity and the magnetic permeability tensors,  $\alpha$  is the magnetolectric coefficient tensor,  $\epsilon$  and  $\sigma$  are the mechanical strain and stress, respectively;  $E$  and  $D$ , are the electrical field and displacement, respectively; and  $H$  and  $B$  are the magnetic field and flux density, respectively.

Multiphysics entities, piezoelectricity, and magnetostriction are included with the coupling of solid mechanics, electrostatics, and magnetic field modules. The magnetic field modelling was performed based on the constitutive B-H relation [16] wherein the boundary condition, *Ampere's Law*, was set for all the domains, except the magnetostrictive material as,

$$\vec{B} = \mu_0 \mu_r \vec{H}, \quad (4)$$

$$\nabla \cdot \vec{H} = \vec{J}, \quad (5)$$

The magnetostriction effect is defined with the boundary condition, *Ampere's Law, Magnetostrictive*, as,

$$\vec{B} = \mu_0 [\vec{H} + \vec{M}(\vec{H}, S_{mech}) + \vec{M}_r], \quad (6)$$

where  $B$  is the magnetic flux density,  $H$  is the magnetic field intensity,  $J$  is the volumetric current density,  $\mu_0$  is the permeability of free space,  $\mu_r$  is the magnetic relative permeability,  $M$  is the magnetization,  $S_{mech}$  is the stress tensor, and  $M_r$  is the remanent magnetization, which is set as zero, since the material will not have residual magnetization after the external source is removed. The magnetostrictive stress is modeled as a non-linear isotropic entity given as,

$$\epsilon_{me} = \frac{3}{2} \frac{\lambda_s}{M_s^2} dev(\vec{M} \otimes \vec{M}), \quad (7)$$

where,  $\lambda_s$  and  $M_s$  are the saturation magnetostriction and magnetization, respectively. The magnetization  $M$ , is given as

a function of effective magnetic field intensity  $H_{eff}$  and  $M_s$  as,

$$\vec{M} = M_s L(|H_{eff}|) \frac{H_{eff}}{|H_{eff}|}, \quad (8)$$

$$\vec{H}_{eff} = \vec{H} + \frac{3\lambda_s}{\lambda_0 M_s^2} S \vec{M}, \quad (9)$$

where,  $L$  is the Langevin function and  $S$  is the stress tensor. For the piezoelectric shell, The *Charge Conservation* boundary condition governs the operating piezo shell given as,

$$\nabla \cdot \vec{F} = \rho_v, \quad (10)$$

where,  $F$  is the electric flux density, and  $\rho_v$  is the volume charge density.

### B. Design and Material Characteristics

In our design, a spherical magnetostrictive core is fully encapsulated inside a spherical piezoelectric material lattice to bind all the mechanical deformation and efficiently transform the energy to shell deformation without free movements, thus ensuring maximum energy coupling between the core and the shell. The shell's piezo lattice is responsible for generating surface charges in response to deformation, validating our energy conversion concept for bio-stimulation. To demonstrate this, a single ME geometry is modelled in COMSOL Multiphysics, illustrating the feasibility of generating a local voltage difference on the piezoelectric shell for potential cell and tissue stimulation. Fig. 3 depicts a schematic of the simulated geometry, where two remote coils and the MEMP are shown. The use of two remote coils facilitates the COMSOL simulation, with each coil applying a specific frequency that combines to form a modulated beating wave in the centre, with a frequency equivalent to the difference between the two applied frequencies ( $\Delta f = f_2 - f_1$ ).

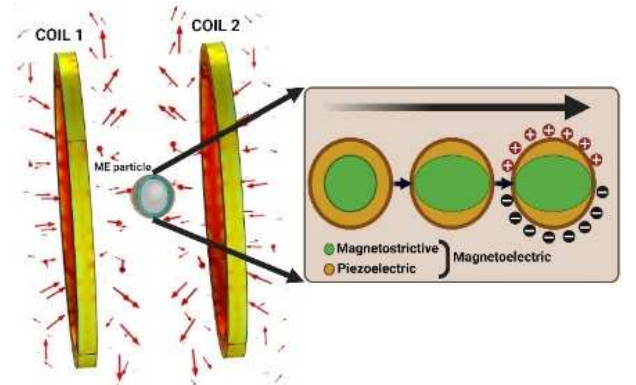


Fig. 3. Simulation setup of the COMSOL geometry showing the coils and the ME device. The magnetic temporal interference frequency (beating wave), which is the difference frequencies of  $f_1$  and  $f_2$ , from coils 1 and 2 respectively, is used to induce magnetostriction in the core, that results in the surface voltage.

The magnetostrictive material is chosen based on the commercially available 2628 MB MetGlas model as the magnetostrictive core [13], known for its high magneto-mechanical coupling coefficient [17]. A piezoelectric coating of Aluminium Nitride (AlN) was added to the magnetostrictive core.

Table 1 provides the material characteristics of MetGlas and AlN, while Table 2 depicts the optimized dimensions of the MEMP. The initial optimization was based on eigenmode

analysis to identify the natural resonance modes of the magnetostrictive material under an applied magnetic field across a wide frequency range. The eigenmode solver identifies the dominant resonance modes and their harmonics, which are not linearly scaled due to the material's nonlinearity at resonances.

To model the piezoelectric material parameters, the material compliance ( $s_E$ ), coupling matrix ( $d$ ), and the permittivity ( $\epsilon_T$ ) are required, and given in Table 3.

Table 1. Material properties of MetGlas (magnetostrictive core) and AlN (piezo shell)

Design geometry	Value
Magnetostrictive core diameter	100 $\mu\text{m}$
Piezoelectric shell thickness	37.5 $\mu\text{m}$
Magnetic field bias	293 mT
Mechanical damping loss in the core and shell	1E-4
Dielectric loss in the piezoshell	1E-4

Table 2. Design geometry of the particle

Material property	MetGlas	AlN [3]
Electrical Conductivity	7.25E5 S/m	1E-6 S/m
Relative Permittivity	1	9
Young's Modulus	152GPa	–
Poisson's ratio	0.22	–
Density	7900 Kg/m <sup>3</sup>	3300 Kg/m <sup>3</sup>
Saturation Magnetization	700282 A/m	–
Saturation Magnetostriction	12 ppm	–

Table 3. Piezoelectric AlN material parameters: material compliance ( $s_E$ ), coupling matrix ( $d$ ), and the permittivity ( $\epsilon_T$ ).

Material compliance $s_E \times 10^{-12} \left(\frac{1}{\text{Pa}}\right)$	Coupling matrix $d \times 10^{-12} \left(\frac{\text{C}}{\text{N}}\right)$	Permittivity $\epsilon_T$
$\begin{bmatrix} 2.9 & -0.93 & -0.5 & 0 & 0 \\ -0.93 & 2.9 & -0.5 & 0 & 0 \\ -0.5 & -0.5 & 2.9 & 0 & 0 \\ 0 & 0 & 0 & 8 & 0 \\ 0 & 0 & 0 & 0 & 8 \\ 0 & 0 & 0 & 0 & 0 \end{bmatrix}$	$\begin{bmatrix} 0 & 0 & 0 & 0 & -3.8 \\ 0 & 0 & 0 & -3.8 & 0 \\ -1.9 & -1.9 & 5 & 0 & 0 \end{bmatrix}$	$\begin{bmatrix} 9 & 0 & 0 \\ 0 & 9 & 0 \\ 0 & 0 & 9 \end{bmatrix}$

The contribution of losses is considered by replacing  $\epsilon_T$  with  $(1 - j \tan \delta) \epsilon_T$  and  $c_E$  with  $(1 + j \eta_s) c_E$  in which  $c_E = S_E^{-1}$ . The loss values are given in Table 1.

Fig. 3 shows the modelling steps. We limited the dimensions of the simulated magnetostrictive core to diameter of 100  $\mu\text{m}$ , making it suitable for use as an injectable device. The modeling methodology employed in our study is depicted in Fig 3. The core shell was placed between two symmetrically positioned coils driven by a constant AC current source of 100 mA. Two mechanical resonant frequencies (168 and 122 MHz) with a considerable frequency difference were selected as the AC excitation of the magnetic fields applied to each coil.

We apply a user-controlled mesh, where triangular mesh is applied for the coil and particle domains, additionally, boundary layer meshing was added to the coil and the particle

boundaries to increase the mesh density distribution. We were able to achieve an average mesh element quality of 0.8496.



Fig 3. Modeling method to analyze the non-linear frequency demodulation and the magnetolectric coupling. Step 1 shows the non-linear variation of Magnetostriction for an applied DC bias sweep. The DC bias field where maximum slope of Magnetostriction is observed, is selected as the Optimum DC bias,  $H_{DC(opt)}$ . Step 2 shows the selection of AC excitation field through Eigen mode analysis. In step 3, we analyze the frequency demodulation at the  $H_{DC(opt)}$ , and the selected AC excitations.

Our numerical methodology relies on a finite element time domain solver, specifically employing the highly nonlinear PARADISO solver settings in COMSOL. To improve computational efficiency, and demonstrate the nonlinear simulation features we selected two AC frequencies with a significant difference of 46 MHz, thus reducing the simulation's time steps and enabling a thorough demonstration of the ME core-shell's nonlinear functionalities.

### III. RESULTS

#### A. DC Bias Selection

The elasticity-induced deformation ( $\lambda$ ) of the magnetostrictive core reaches its maximum when the optimal static magnetic bias,  $H_{DC(opt)}$ , is applied. For the chosen MetGlas material and dimensions, the strain is constrained within the range of  $\{-0.88, 0.88\}$  T. The optimal bias field is initially identified between 200 – 350 mT, which is the range where the curve's slope is at its maximum (Fig...). This bias field is later fine-tuned to 293 mT to achieve the highest magneto-electric coupling efficiency.

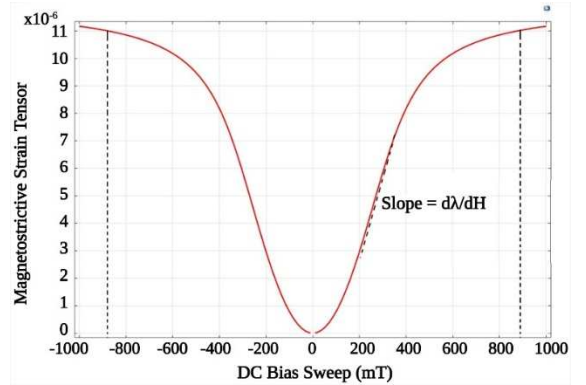


Fig 4. Non-linear magnetization curve showing the rise and fall magnetostrictive strain at  $\approx \{-0.88, 0.88\}$  T and the maximum slope of the magnetostriction in the range 200 – 350 mT.

#### B. Selection of AC Excitation Field

At magneto-mechanical resonant frequencies, the magnetostrictive core of the particle exhibits maximum deformation, identifiable by its eigenmode frequencies. Here, the core experiences intense, irregular deformation in relation to the applied magnetic field frequency. Our analysis focused on identifying optimal resonant frequencies (within the 30 – 240 MHz range) for the magnetostrictive sphere of 100  $\mu\text{m}$ , with  $H_{DC(opt)}$  set at 293 mT, where the damping ratio is

minimized. Fig. 5 shows the particle surface deformation in the frequency range of 30 – 240 MHz. Fig. 6 shows the damping ratio ( $\delta = \frac{\text{imag}(freq)}{\text{abs}(freq)}$ ) for the frequency range. A lower damping ratio provides a higher quality factor (Q-factor) in particle resonance with minimum loss. Two specific frequencies, 168 MHz and 122 MHz, were chosen due to their significant difference and lower damping ratios ( $< 10^{-10}$ ), which facilitate maximal mechanical deformation. This selection aims to streamline numerical computations for validating non-linearity and wave demodulation.

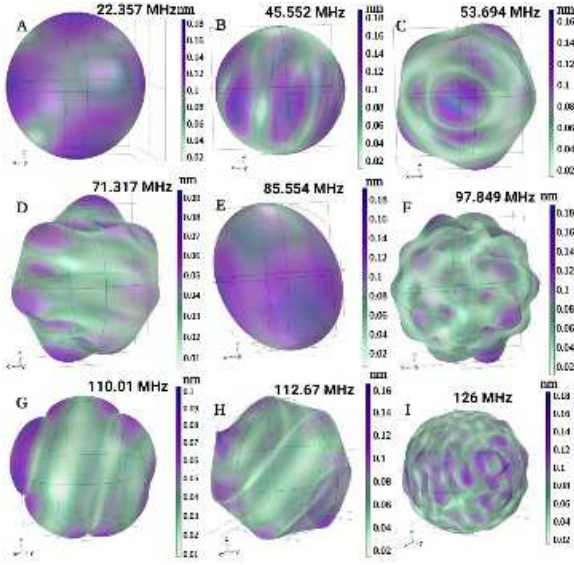


Fig. 5. Particle surface deformation forming ‘Electrical Hotspots.’

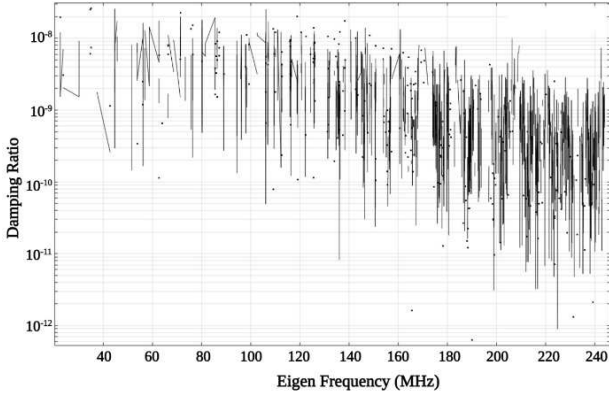


Fig. 6. Damping ratio variation for the applied AC frequencies.

For practical applications in neural stimulation, the frequency difference should fall below 500 Hz for effective neuromodulation, meaning one of these frequencies may be sufficient as the resonance bandwidth is adequate to support low-frequency demodulation [18].

### C. Non-linear Magnetostriction induced Frequency Demodulation

The choice of two distinct frequencies primarily aids in reducing computation time within the simulation framework. In our study, we conducted a time-domain simulation of the magnetostrictive core using dual-frequency magnetic field applications and a DC bias. The magnetic field near the particle surface was sampled over time, and Fourier transform analysis was utilized to investigate the effects of

magnetostrictive non-linearity on magnetic field intensity variations. The recorded magnetic field results from the interaction of two applied source frequencies with the material.

As shown in Fig. 7, this interaction leads to a multiplication of the applied frequencies, generating a new frequency due to waveform deformation. The frequency of these components is the difference frequency of the applied waveforms.

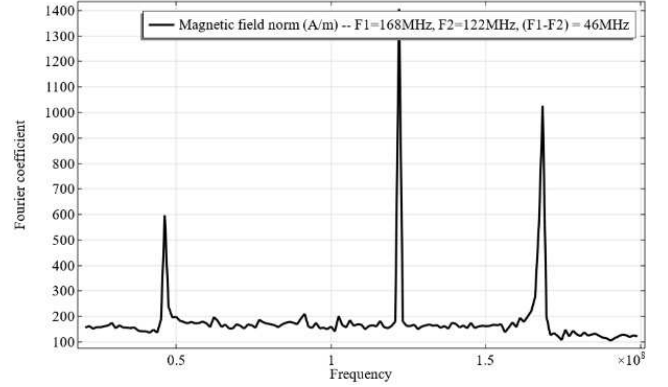


Fig. 7. Frequency demodulation with two applied frequencies ( $\Delta f = f_2 - f_1$ ), computed with COMSOL modeling

The recorded magnetic field is the result of the magnetostrictive mechanical deformation, which is coupled to a piezo electric shell that is linearly coupled with the mechanical structure and converts the deformation to electric charges on the piezo surface. It is important that the mechanical resonances of the two parts are aligned for maximum q-factor with minimum loss. For this reason we have designed the shell coating thickness with the goal of maximizing the magneto-electric coupling factor.

### D. Magnetolectric Coupling Factor ( $\alpha_{ME}$ )

The magnetolectric (ME) coupling factor, denoted as  $\alpha_{ME}$ , is a vital metric for understanding the interactions among the magnetic, elastic, and electric domains within the core-shell structure. This factor quantifies the transformation of induced magnetization into electrical polarization and is mathematically defined as:

$$\alpha_{ME} = \frac{dE}{dH} \left( \frac{V}{m} \cdot Oe \right) \quad (8)$$

where E represents the electrical field in the piezoelectric layer, and H represents the magnetic field in the magnetostrictive layer. Fig. 8 shows the  $\alpha_{ME}$  versus applied magnetic bias and piezo shell thickness at the difference frequency, meaning the demodulated wave.

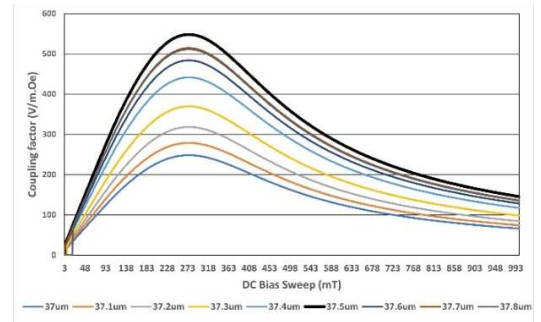


Fig. 8. Variation of coupling factor  $\alpha_{ME}$  for an applied  $H_{DC}$

The optimum value of shell thickness 37.5  $\mu\text{m}$  identifies the optimal coupling coefficient. We observed a peak coupling factor of approximately  $\alpha_{ME} = 550 \frac{\text{V}}{\text{m}} \cdot \text{Oe}$ . Interestingly, within the operational DC bias range of 200 – 350 mT,  $\alpha_{ME}$  reaches its peak, implying maximum conversion efficiency.

#### E. Hodgkin–Huxley Bio-Stimulation Model

The process of transferring piezoelectric charges to a biological medium for potential neural stimulation has been modelled using the Hodgkin-Huxley neural model [19]. This model indicates the required electric field intensity for efficient neural stimulation. COMSOL Multiphysics was used to model the effect of induced current ( $i_{ind}$ ) from the MEMP, on the HH neural model.

The general governing equation for the membrane potential in the HH model () was modified with the  $i_{ind}$  as,

$$\frac{dv_m}{dt} = -\frac{1}{C_m} [g_K(v_m - V_K) + g_{Na}(v_m - V_{Na}) + g_L(v_m - V_L) - i_{ind}] \quad (7)$$

where  $C_m$  is specific membrane capacitance;  $V_K$ ,  $V_{Na}$ , and  $V_L$  are Nernst potentials for  $K^+$  ions;  $Na^+$  and other ions are combined as “leak” channels; and  $g_K$ ,  $g_{Na}$ , and  $g_L$  are the corresponding membrane conductance. Voltage-gated conductance  $g_K = \bar{g}_K m_K^4$  and  $g_{Na} = \bar{g}_{Na} m_{Na}^3 h_{Na}$  change with time during an action potential.  $m_K^4$  and  $m_{Na}^3$  represent the opening probabilities for  $K^+$  and  $Na^+$  channels, respectively.

The gating variables,  $m_K$ ,  $m_{Na}$  and  $h_{Na}$  steady state equations and the gating functions are fixed values and could be referred here [20] (in Section 1.9 and 1.10 of the cited reference). The general parameters used to compute the membrane potential  $v_m$  is given in Table 4.

Table 4. Parameters that quantify the electrical activity of a neuron

Parameter	Nominal Value	Unit
Initial membrane conductance, Potassium channel ( $\bar{g}_K$ )	36	mS/cm <sup>3</sup>
Nernst potential, Potassium channel ( $V_K$ )	-70	mV
Initial membrane conductance, Sodium channel ( $\bar{g}_{Na}$ )	120	mS/cm <sup>3</sup>
Nernst potential, Sodium channel ( $V_{Na}$ )	50	mV
Initial membrane conductance, other ion channels ( $g_L$ )	0.3	mS/cm <sup>3</sup>
Combined Nernst potential, other ion channels ( $V_L$ )	-54.4	mV
Specific membrane capacitance ( $C_m$ )	1	$\mu\text{F}/\text{cm}^3$

The current density value from our previous ME coreshell simulation was interpolated and included as a piecewise function which was then included in (7).

Fig. 9 shows the generated single spike of the membrane potential.

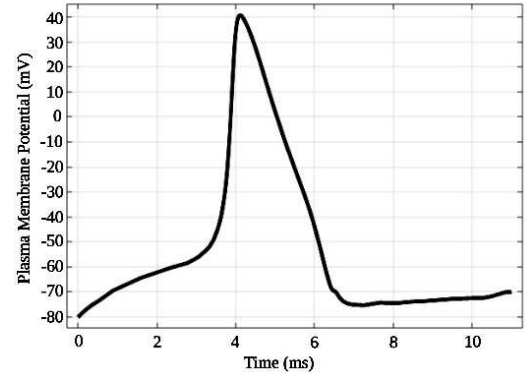


Fig. 9. Generated membrane potential through the induced stimulation current  $i_{ind}$ . The repolarization and depolarization phases of the signal are in accordance with the membrane potential shown in the reference here [21] (Page 32, Figure 4.1).

#### IV. CONCLUSION

In this work, we simulated the low-frequency demodulation and the electrical field generation of ME microparticles. We showed that through the optimal selection of materials and the structural dimension of the core-shell, the maximal ME coupling factor of  $550 \frac{\text{V}}{\text{m}} \cdot \text{Oe}$  was achieved. We also showed that an optimum generated current density of  $\sim 8 - 18 \mu\text{A}/\text{cm}^2$  could stimulate the tissue surface under consideration, from a spatial distance of  $\sim 20 - 30 \mu\text{m}$ . Moreover, we also fed the current density values we acquired from the ME microparticle simulation to a Hodgkin-Huxley model to demonstrate the generation of spiking potential in the nerve cell.

Powering biomedical implants is a focused research field with multiple research areas like micro/nano photonic, optical, pressure-based, and electro-mechanical sources, etc. The physics of ME structures could be tapped to provide an electronics-free capability to compensate for the power requirements of such implants. Through this work, we have introduced a simulation proof-of-concept for a battery and electronics-free implantable ME microparticles. We have presented a use case for a self-electrical field-induced stimulation microdevice using ME particles. Moreover, the ME device's ability to demodulate and utilize the low-frequency electrical fields for stimulation opens avenues of research to use the demodulation effect for a range of biomedical applications in the future, including frequency-divided communication channels, low-frequency magnetic fields induced drug delivery, etc.

This study demonstrates the potential of using a modulated magnetic field with non-linear magnetoelectric (ME) core shells for stimulating biological cells and tissues. By fine-tuning the geometry, magnetic bias, and excitation frequencies, these ME core shells can precisely localize electric fields for effective stimulation. Our method offers enhanced spatial resolution and energy efficiency removing potential electronics and wires in traditional bio stimulation. While promising remote neural stimulation applications, such as deep brain stimulation, further research is needed to evaluate its thermal effects and safety. Future work will also explore the broader biomedical applications of this technology.

## REFERENCES

- [1] M. Zhang, Z. Tang, X. Liu, and J. der Spiegel, "Electronic neural interfaces," *Nat. Electron.*, vol. 3, no. 4, pp. 191–200, 2020.
- [2] H. R. Siebner *et al.*, "Transcranial magnetic stimulation of the brain: What is stimulated?—a consensus and critical position paper," *Clin. Neurophysiol.*, vol. 140, pp. 59–97, 2022.
- [3] Z. Jafari, B. E. Kolb, and M. H. Mohajerani, "Neural oscillations and brain stimulation in Alzheimer's disease," *Prog. Neurobiol.*, vol. 194, p. 101878, 2020.
- [4] M. Verdes, K. Mace, L. Margetts, and S. Cartmell, "Status and challenges of electrical stimulation use in chronic wound healing," *Curr. Opin. Biotechnol.*, vol. 75, p. 102710, Jun. 2022, doi: 10.1016/j.copbio.2022.102710.
- [5] H. Soliman and G. Gourcerol, "Gastric Electrical Stimulation: Role and Clinical Impact on Chronic Nausea and Vomiting," *Front. Neurosci.*, vol. 16, p. 909149, May 2022, doi: 10.3389/fnins.2022.909149.
- [6] S. J. H. Van Rooij, A. R. Arulpragasam, W. M. McDonald, and N. S. Philip, "Accelerated TMS—moving quickly into the future of depression treatment," *Neuropsychopharmacology*, vol. 49, no. 1, pp. 128–137, 2024.
- [7] J. A. Camacho-Conde, M. del R. Gonzalez-Bermudez, M. Carretero-Rey, and Z. U. Khan, "Brain stimulation: a therapeutic approach for the treatment of neurological disorders," *CNS Neurosci. Ther.*, vol. 28, no. 1, pp. 5–18, 2022.
- [8] J. M. Stilling, O. Monchi, F. Amoozegar, and C. T. Debert, "Transcranial magnetic and direct current stimulation (TMS/tDCS) for the treatment of headache: A Systematic Review," *Headache J. Head Face Pain*, vol. 59, no. 3, pp. 339–357, 2019.
- [9] C. Wu *et al.*, "A Bioactive and Photoresponsive Platform for Wireless Electrical Stimulation to Promote Neurogenesis," *Adv. Healthc. Mater.*, vol. 11, no. 20, p. 2201255, Oct. 2022, doi: 10.1002/adhm.202201255.
- [10] A. Singer *et al.*, "Magnetolectric materials for miniature, wireless neural stimulation at therapeutic frequencies," *Neuron*, vol. 107, no. 4, pp. 631–643, 2020.
- [11] J. C. Chen *et al.*, "Self-rectifying magnetolectric metamaterials for remote neural stimulation and motor function restoration," *Nat. Mater.*, pp. 1–8, 2023.
- [12] A. Jahanshahi, K. Kozielski, Y. Temel, and M. Sitti, "Wireless deep brain stimulation in freely moving mice with nonresonant powering of magnetolectric nanoparticles," *Brain Stimul. Basic, Transl. Clin. Res. Neuromodulation*, vol. 14, no. 6, p. 1742, 2021.
- [13] M. Zaeimbashi *et al.*, "NanoNeuroRFID: A Wireless Implantable Device Based on Magnetolectric Antennas," *IEEE J. Electromagn. RF Microwaves Med. Biol.*, vol. 3, no. 3, pp. 206–215, 2019, doi: 10.1109/JERM.2019.2903930.
- [14] I. Bok, I. Haber, X. Qu, and A. Hai, "In silico assessment of electrophysiological neuronal recordings mediated by magnetolectric nanoparticles," *Sci. Reports 2022 121*, vol. 12, no. 1, pp. 1–14, May 2022, doi: 10.1038/s41598-022-12303-4.
- [15] M. Zaeimbashi *et al.*, "Ultra-compact dual-band smart NEMS magnetolectric antennas for simultaneous wireless energy harvesting and magnetic field sensing," *Nat. Commun. 2021 121*, vol. 12, no. 1, pp. 1–11, May 2021, doi: 10.1038/s41467-021-23256-z.
- [16] Y. Wang, Y. Su, J. Li, and G. J. Weng, "A theory of magnetolectric coupling with interface effects and aspect-ratio dependence in piezoelectric-piezomagnetic composites," *J. Appl. Phys.*, vol. 117, no. 16, 2015, doi: 10.1063/1.4919016.
- [17] S. W. Meeks and J. C. Hill, "Piezomagnetic and elastic properties of metallic glass alloys Fe<sub>67</sub>Co<sub>18</sub>B<sub>14</sub>Si<sub>1</sub> and Fe<sub>81</sub>B<sub>13</sub>.5Si<sub>3.5</sub>C<sub>2</sub>," *J. Appl. Phys.*, vol. 54, no. 11, pp. 6584–6593, 1983, doi: 10.1063/1.331893.
- [18] S. F. Cogan, "Neural stimulation and recording electrodes," *Annu. Rev. Biomed. Eng.*, vol. 10, pp. 275–309, 2008.
- [19] A. L. Hodgkin and A. F. Huxley, "A quantitative description of membrane current and its application to conduction and excitation in nerve," *J. Physiol.*, vol. 117, no. 4, pp. 500–544, Aug. 1952, doi: 10.1113/JPHYSIOL.1952.SP004764.
- [20] B. Ermentrout and D. H. Terman, *Foundations of mathematical neuroscience*. Citeseer, 2010.
- [21] J. M. Bower and D. Beeman, *The book of GENESIS: exploring realistic neural models with the GENeral NEural Simulation System*. Springer Science & Business Media, 2012.